Vol. 24, No. 2(2025) Sim25480
Revista Mexicana de Ingeniería Química

Numerical analysis of ilmenite particle diameter on thermal and fluid dynamic behavior in a chemical looping combustion system

Análisis numérico del diámetro de partículas de ilmenita sobre el comportamiento térmico y fluidodinámico en un sistema de combustión en ciclos químicos

F.A. Ocampo-Vaca[1], C. A. Hernández-Bocanegra[2*], R. Maya-Yescas[1] and J. A. Ramos-Banderas [2]
[1]Faculty of Chemical Engineering, Universidad Michoacana de San Nicolás de Hidalgo, Morelia, Michoacán, México.
[2]National Technological Institute of Mexico, Morelia Campus, Morelia, Michoacá, México.
Received: November 29, 2024; Accepted: March 5, 2025

Abstract
This study utilized numerical simulation to analyze the effect of particle diameter on the fluid dynamics within a chemical looping combustion (CLC) system consisting of two interconnected fluidized bed reactors. The non-isothermal multiphase Eulerian model was employed to simulate ilmenite particles as the granular phase in the CLC system, aiming to investigate the impact of particle diameters of 80 μm, 120 μm, 150 μm, 180 μm, 220 μm, and 270 μm on their distribution within the reactor system. The results demonstrated that particle diameter is a critical variable, significantly influencing their distribution. For particles measuring 80 μm and 120 μm, the drag force generated by the airflow predominates, resulting in complete entrainment of the granular phase in the air reactor. In the cases of particles with diameters between 150 μm and 180 μm, the drag force is counterbalanced by gravitational force and for particles with diameters of 220 μm and larger gravitational force exceeds drag force for particles with diameters of 220 μm and larger, rendering them unsuitable for use within this system. Finally, regarding temperature the results showed less cooling of the system when 150 μm particles were used.
Keywords: Chemical looping combustion, CO_2 emissions, particle flow, numerical simulation.

Resumen
Este estudio utilizó simulación numérica para analizar el efecto del diámetro de partículas sobre la fluidodinámica dentro de un sistema de combustión en ciclos químicos (CLC, por sus siglas en inglés) compuesto por dos reactores de lecho fluidizado interconectados. Mediante un modelo euleriano multifásico no isotérmico, se simularon partículas de ilmenita como fase granular, evaluando diámetros de 80 μm, 120 μm, 150 μm, 180 μm, 220 μm y 270 μm para analizar su distribución en el sistema. Los resultados mostraron que el diámetro de las partículas es crítico, afectando significativamente su comportamiento. Las partículas de 80 μm y 120 μm fueron completamente arrastradas por el flujo de aire en el regenerador, mientras que para diámetros entre 150 μm y 180 μm, la fuerza de arrastre fue equilibrada por la gravedad. En partículas de 220 μm o mayores, la fuerza gravitacional superó la de arrastre, haciéndolas inadecuadas para este sistema. Respecto a la temperatura, las partículas de 150 μm resultaron en un menor enfriamiento del sistema, mostrando un comportamiento óptimo en comparación con los otros diámetros evaluados.
Palabras clave: Combustión en ciclos químicos, emisiones de CO_2, flujo de partículas, simulación numérica.

*Corresponding author. *E-mail*: constantin.hb@morelia.tecnm.mx ;
https://doi.org/10.24275/rmiq/Sim25480
ISSN:1665-2738, *issn-e*: 2395-8472

1 Introduction

It is well known that since the Industrial Revolution, humanity's energy consumption has grown exponentially. Fossil fuels have been the primary energy sources used since then, primarily due to their low cost and ease of handling. Fossil fuels account for approximately 85% of global energy consumption (Kumar & Muhuri, 2019). Since the mid-20th century, this widespread use of fossil fuels, along with the resulting carbon dioxide (CO_2) emissions, has been considered one of the primary causes of climate change (Kumar & Muhuri, 2019) (Stocker, *et al*., 2013). Greenhouse gases are classified as direct and indirect based on their induction of radiative forcing. Direct greenhouse gases are those that induce global warming and are responsible for the increase in planetary temperature as well as regional climate variability. These include carbon dioxide (CO_2), methane (CH_4), nitrous oxide (N_2O), hydrofluorocarbons, perfluorocarbons, and sulfur hexafluoride (SF_6). On the other hand, indirect greenhouse gases impact atmospheric chemistry by altering the lifespan of direct greenhouse gases in the atmosphere (Martínez-Prado, M. A., 2016). CO_2 accounts for nearly 75% of anthropogenic gas emissions (Adanez, Abad, Garcia-Labiano, Gayan, & De Diego, 2012), with an estimated atmospheric lifespan of approximately 12 years (Archer & Jacobson, 2005). Climate change is a recognized phenomenon, and its most detrimental impact is the potential alteration of the biodiversity of Earth (Gitay, 2002). By 2017, human-induced global warming had reached approximately 1°C above pre-industrial levels, with the planet's temperature increasing at 0.2°C per decade (Masson-Delmotte, *et al*., 2018). It is estimated that by 2045, fossil fuels will remain a significant energy source (Pugazhendhi, *et al*., 2019), meaning that energy generation and climate change are closely connected and require a holistic solution (Höök & Tang, 2013). One alternative that combines the necessity of using fossil fuels with the urgency of reducing CO_2 emissions to the atmosphere is Chemical Looping Combustion (CLC) systems. This process involves two interconnected fluidized bed reactors. In the first reactor, called the fuel reactor, syngas ($CO + H_2$) is fully oxidized in the absence of air, using oxygen carried by the natural metal oxide known as ilmenite ($Fe^{2+}Ti^{4+}O_2$), which is simultaneously reduced. In the second air reactor, the carrier is oxidized again through contact with air. The fuel reactor operates in a bubbling regime, while the air reactor operates in a particle entrainment or riser regime.

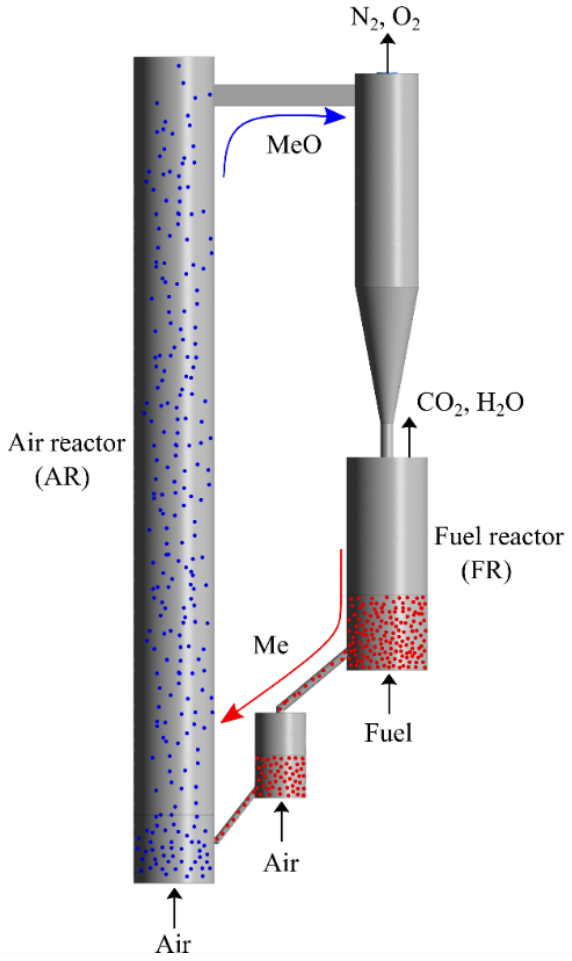

Figure 1. Scheme of the CLC process.

For this reason, these processes do not involve high economic costs for CO_2 capture. Figure 1 shows a diagram of the CLC process. In its special report on carbon dioxide capture and storage (2005), the IPCC identified chemical looping combustion as one of the cheapest technologies for CO_2 capture, especially when complementing power generation plants (Kerr, 2005) (Deng Z., Xiao, Jin, Song, & Huang, 2008). The main drawback of CLC is the low confidence level due to the lack of technological maturity, which presents a significant opportunity to study chemical looping combustion.

Various mathematical simulation studies of particle flow have been developed to study the CLC process, some of them focusing solely on the fuel reactor (Deng *et al*., 2009; Jin *et al*., 2009; Jung & Gamwo, 2008; Mahalatkar *et al*., 2011; Shuai *et al*., 2011). In other studies, the complete CLC system has been examined, that is, both the fuel reactor and the air reactor (Kruggel-Emden *et al*., 2010; Nguyen *et al*., 2012; Seo *et al*., 2011; Shuai *et al*., 2011; Shuai *et al*., 2014). This work stands out from previous research because it analyzes an aspect that has been relatively underexplored in the existing literature: the variation in the diameter of oxygen-carrying particles

Table 1. Summary of studies related to particle size in CLC.

Reference	Year	System	Particle diameter (μm)
Peirano *et al*. [21]	2001	Fluidized bed	283
Jung & Gamwo [11]	2008	FR	120
Deng *et al*. [12]	2009	FR	275
Kruggel-Emden *et al*. [16]	2010	FR + AR	150
Shuai *et al*. [22]	2011	FR + AR	150
Shuai *et al*. [18]	2011	FR	120
Mahalatkar *et al*. [15]	2011	FR	128
Kruggel-Emden *et al*. [23]	2011	FR	150
Seo *et al*. [19]	2011	FR	250
Nguyen *et al*. [20]	2012	FR + AR	250
Shuai *et al*. [18]	2014	FR + AR	135
Guan *et al*. [24]	2014	FR + AR	150
Bougamra *et al*. [25]	2014	FR + AR	200
Alobaid *et al*. [26]	2015	FR	120
Porrazzo *et al*. [27]	2016	FR	200
Zhang *et al*. [28]	2017	FR + AR	135
Sornumpol *et al*. [29]	2017	FR	150 and 175
May *et al*. [30]	2018	FR + AR	300
Lin *et al*. [31]	2019	FR	200
Li and Shen [32]	2021	AR	140

and its impact on the fluid dynamic distribution of both the granular phase and the continuous phase, as well as on the distribution and thermal profiles within chemical looping combustion systems. In many prior studies, a single diameter value has been employed (Table 1), which limits understanding how variations in this parameter can influence system behavior. By analyzing multiple particle diameters, this research expands knowledge about fluidization dynamics and provides a more realistic and applicable approach to practical situations. Examining how the variation in particle diameter affects their distribution can help optimize the performance of chemical looping combustion systems, promoting a more effective and sustainable operation. This work enhances the current knowledge in chemical looping combustion and contributes to improving cleaner and more efficient technologies.

2 Methodology

2.1 *Domain dimensions, boundary conditions and assumptions*

The simulation was conducted considering the geometry of a chemical looping combustion process at scale, taken from the work of Guan *et al*. (Guan, Chang, Zhang, Wang, & Sun, 2014). Figure 2(a) shows the model's dimensions, and Figure 2 (b) shows the phases and boundary conditions.

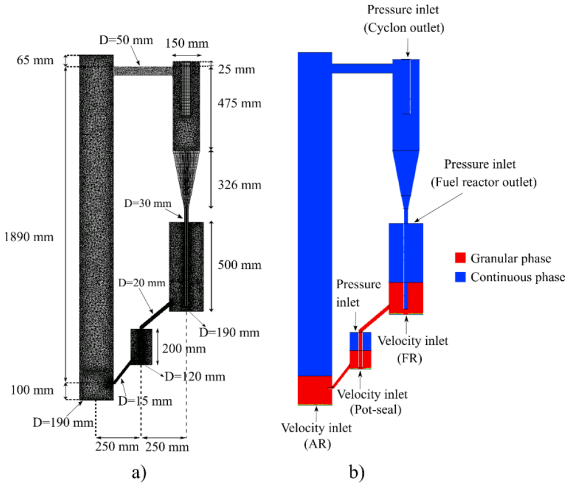

Figure 2. a) Mesh and dimensions of the model and b) Boundary conditions.

The mesh of the computational domain consisted of 697,584 elements. This mesh was determined through a mesh sensitivity analysis, shown in Figure 3, where the fluid velocity in the air reactor was analyzed for four different meshes. Based on this analysis, mesh 3, corresponding to 697,584 elements, was used since, as shown in Figure 3, the velocity profiles of meshes 3 and 4 are practically superimposed on one another. This analysis allowed us to conclude that the results are no longer affected by the number of elements in the mesh, and there is no point in using meshes with a more significant number of elements. Tables 2 and 3 show the properties of the materials used in the numerical simulation of the multiphase system, as well

Table 2. Thermo-physical properties of materials.

Property	Value	Units
Fluid phase density	1.225	$kg \cdot m^{-3}$
Granular phase density	2600	$kg \cdot m^{-3}$
Fluid phase viscosity	1.7894×10^{-5}	$kg \cdot m^{-1} \cdot s^{-1}$
Granular phase viscosity	Kinetic theory	$kg \cdot m^{-1} \cdot s^{-1}$
Fluid phase specific heat	1006.43	$J \cdot kg^{-1} \cdot K^{-1}$
Granular phase specific heat	Kinetic theory	$J \cdot kg^{-1} \cdot K^{-1}$
Fluid phase thermal conductivity	0.0242	$W \cdot m^{-1} \cdot K^{-1}$
Granular phase thermal conductivity	Kinetic theory	$W \cdot m^{-1} \cdot K^{-1}$

Table 3. Operation parameters and boundary conditions.

Parameter	Value	Units
Inventory of solids in the system	17.5	kg
Velocity inlet in AR	0.9	$m \cdot s^{-1}$
Velocity inlet in FR	0.08	$m \cdot s^{-1}$
Velocity inlet in pot-seal	0.002	$m \cdot s^{-1}$
Pressure inlet	1	atm
Initial temperature of granular phase	1273	K

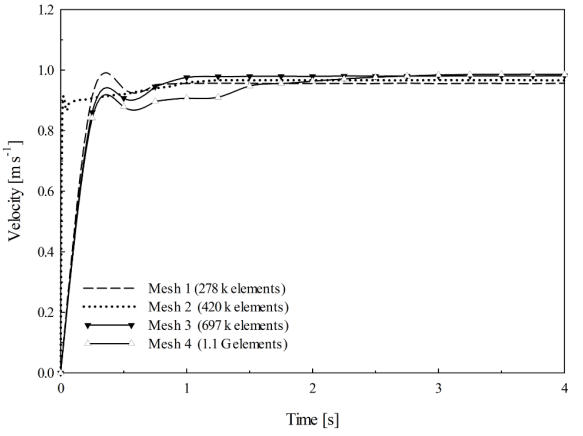

Figure 3. Mesh sensitivity analysis study.

as the system's operating parameters and boundary conditions.

2.2 *Governing equations*

The Eulerian model is the most complex and robust of the multiphase models. In this model, the volume fractions represent the space occupied by each phase (gas phase and solid phase). The principles of mass and momentum conservation are solved individually for each phase. Coupling is achieved through pressure and exchange coefficients at the interface; for granular flows (fluid-solid), the properties are obtained through the application of kinetic theory.

2.2.1 *Continuity equations*

The mass conservation equation is described by equation 2.1 (ANSYS, 2013):

$$\frac{\partial}{\partial t}\left(\alpha_q \rho_q\right) + \nabla \cdot \left(\alpha_q \rho_q \vec{v}_q\right) = \sum_{p=1}^{n} \left(\dot{m}_{pq} - \dot{m}_{qp}\right) + S_q \quad (1)$$

Here ρ_q is the density, $\vec{v}_q$ is the velocity vector, and α_q is the volume fraction, with the subscript q representing phase q, m_{pq} characterizes the mass transfer from the p^{th} to q^{th} phase, and $\dot{m}_{qp}$ characterizes the mass transfer from the q^{th} to p^{th}. The term S_q is a mass source term for cases where chemical reactions are present.

2.2.2 *Conservation equations of momentum for both phases*

The balance of forces for phase q is described by equation 2.2 (ANSYS, 2013):

$$\frac{\partial}{\partial t}\left(\alpha_q \rho_q \vec{v}_q\right) + \nabla \cdot \left(\alpha_q \rho_q \vec{v}_q \vec{v}_q\right) = -\alpha_q \nabla P + \nabla \cdot \bar{\bar{\tau}}_q + \alpha_q \rho_q \vec{g} + \sum_{p=1}^{n} \left(R_{pq}\left(\vec{v}_p - \vec{v}_q\right) + \dot{m}_{pq}\vec{v}_{pq} - \dot{m}_{qp}\vec{v}_{qp}\right) + \left(\vec{F}_q + \vec{F}_{lift,q} + \vec{F}_{wl,q} + \vec{F}_{vm,q} + \vec{F}_{td,q}\right) \quad (2)$$

Here $\bar{\bar{\tau}}_q$ is the q^{th} phase stress-strain tensor:

$$\bar{\bar{\tau}}_q = \alpha_q \mu_q \left(\nabla \vec{v}_q + \nabla \vec{v}_q^{T}\right) + \alpha_q \left(\lambda_q - \frac{2}{3}\mu_q\right) \nabla \cdot \vec{v}_q \bar{\bar{I}} \quad (3)$$

Here μ_q and λ_q are the shear and bulk viscosity of phase q, $\vec{F}_q$ is an external body force, $\vec{F}_{lift,q}$ is a lift force, $\vec{F}_{wl,q}$ is a wall lubrication force, $\vec{F}_{vm,q}$ is a virtual mass force and $\vec{F}_{td,q}$ is a turbulent dispersion force. R_{pq} is an interaction force between phases, and P is the pressure shared by all phases. $\vec{v}_{pq}$ is the interphase velocity, defined as follow, If $\dot{m}_{pq} > 0$ (that is, phase p mass is being transferred to phase q), $\vec{v}_{pq} = \vec{v}_p$; if $\dot{m}_{pq} < 0$ (that is, phase q mass is being transferred to phase p) $\vec{v}_{pq} = \vec{v}_q$. Likewise, if $\dot{m}_{qp} > 0$ then $\vec{v}_{qp} = \vec{v}_q$; if $\dot{m}_{qp} < 0$ then $\vec{v}_{qp} = \vec{v}_p$.

2.2.3 Energy equations

$$\frac{\partial}{\partial t}\left(\alpha_q \rho_q \bar{h}_q\right) + \nabla \cdot \left(\alpha_q \rho_q \bar{u}_q h_q\right) = \alpha_q \frac{\partial p_q}{\partial t} + \bar{\bar{\tau}}_q + \nabla \bar{u}_q - \nabla \cdot \bar{q}_q + S_q + \sum_{p=1}^{n} (Q_{pq} + \dot{m}_{pq} h_{pq} - \dot{m}_{qp} h_{qp}) \quad (4)$$

here, h_q is the specific enthalpy of the phase q, $\bar{q}_q$ is the heat flux, S_q is the source term, Q_{pq} represents the intensity of heat exchange between the phases and h_{pq} is the interfacial enthalpy.

2.2.4 Standard $\kappa - \varepsilon$ turbulence model (Launder & Spalding, 1983)

The robustness, economy, and reasonable accuracy for many turbulent flows explain the popularity of this model in fluid flow simulations (5) (6).

$$\frac{\partial}{\partial t}(\rho k) + \frac{\partial}{\partial x_i}(\rho k u_i) = \frac{\partial}{\partial x_j}\left[\left(\mu + \frac{\mu_t}{\sigma_k}\right)\frac{\partial k}{\partial x_j}\right] + G_k + G_b - \rho\varepsilon - Y_M + S_k \quad (5)$$

$$\frac{\partial}{\partial t}(\rho \varepsilon) + \frac{\partial}{\partial x_i}(\rho \varepsilon u_i) = \frac{\partial}{\partial x_j}\left[\left(\mu + \frac{\mu_t}{\sigma_\varepsilon}\right)\frac{\partial \varepsilon}{\partial x_j}\right] + C_{1\varepsilon}\frac{\varepsilon}{k}(G_k + C_{3\varepsilon}G_b) - C_{2\varepsilon}\rho\frac{\varepsilon^2}{k} + S_\varepsilon \quad (6)$$

where G_k is the generation of turbulent kinetic energy, G_b is the generation of turbulent kinetic energy, Y_M is the contribution of the fluctuating dilatation. $C_{1\epsilon}$, $C_{2\epsilon}$ and $C_{3\epsilon}$ are model constants. σ_k *y* σ_ε are the turbulent Prandtl numbers for k and for ε, respectively. S_k and S_ε are the source terms.

2.3 Models for granular properties

It is necessary to calculate granular properties when using the Eulerian multiphase model for a granular phase. The employed software provides various models that can be employed for each of these properties.

2.3.1 Granular viscosity

Syamlal *et al* (ANSYS, 2013):

$$\mu_s = \frac{\alpha_s d_s \rho_s \sqrt{\theta_s \pi}}{6(3 - e_{ss})}\left[1 + \frac{2}{5}(1 + e_{ss})(3e_{ss} - 1) g_0 \alpha_s\right] \quad (7)$$

2.3.2 Bulk viscosity

The solids bulk viscosity considers the resistance of the granular phase to compression and expansion (Lun, Savage, Jeffrey , & Chepurniy, 1984):

$$\lambda_s = \frac{4}{3}\alpha_s^2 \rho_s d_s g_0 (1 + e_{ss})\left(\frac{\theta_s}{\pi}\right)^{1/2} \quad (8)$$

2.3.3 Solids pressure

The total solids pressure is calculated and included in the momentum conservation equations. The total solids pressure is the sum of the solids pressure for each solid phase:

$$P_{s,total} = \sum_{q=1}^{n} p_q \quad (9)$$

The solids pressure formulation consists of a kinetic term and a second term corresponding to particle collisions:

$$P_s = \alpha_s \rho_s \theta_s + 2\rho_s (1 + e_{ss}) \alpha_s^2 g_{0,ss} \theta_s \quad (10)$$

Here, e_{ss} is the coefficient of restitution for particle collisions, $g_{0,ss}$ is the radial distribution function, and θ_s is the granular temperature.

2.3.4 Granular temperature

The granular temperature of the solid phase is proportional to the kinetic energy of the particles' random motion.

$$\theta_s = \frac{1}{3} u_s, i u_{s,i} \quad (11)$$

Here, $iu_{s,i}$ represents the component of the fluctuating velocity of the solids in the Cartesian coordinate system. This is defined as an ensemble average of the random velocity of particles within a finite volume over a period of time.

The transport equation derived from kinetic theory takes the form:

$$\frac{2}{3}\left[\frac{\partial}{\partial t}(\rho_s \alpha_s \theta_s) + \nabla \cdot (\rho_s \alpha_s v_s \theta_s)\right] = \left(-p_s \bar{\bar{I}} + \bar{\bar{\tau}}_s\right) : \nabla \bar{v}_s + \nabla \cdot (k_{\theta_s} \nabla \theta_s) - \gamma_{\theta_s} + \varphi_{ls} \quad (12)$$

Here, $\left(-p_s \bar{\bar{I}} + \bar{\bar{\tau}}_s\right) : \nabla \bar{v}_s$ is the generation of energy by the solid stress tensor, $k_{\theta_s} \nabla \theta_s$ is the energy diffusion term, γ_{θ_s} represents energy dissipation due to collisions and φ_{ls} represents energy exchange between the continuous and granular phases.

Equation (13) contains the term $k_{\theta_s} \nabla \theta_s$, which describes the diffusion of the granular flow. When using the default Syamlal *et al*. model (Syamlal, Rogers, & O'Brien, 1993), the diffusion coefficient is given by:

$$k\theta_s = \frac{15 d_s \rho_s \alpha_s \sqrt{\theta_s \pi}}{4(41 - 33\eta)}\left[1 + \frac{12\eta^2}{5}(4\eta - 3)\alpha_s g_0 + \frac{16}{15\pi}(41 - 33\eta)\eta \alpha_s g_0\right] \quad (13)$$

2.3.5 Radial distribution function

The radial distribution function is a correction factor that modifies the probability of collisions between grains when the granular solid phase becomes dense.

$$g_0 = \frac{s + d_p}{s} \tag{14}$$

Here, s is the distance between grains.

2.3.6 Frictional viscosity

In dense flows where the volume fraction of the secondary phase approaches the packing limit, stress generation is mainly due to friction between particles. Frictional viscosity is included through the Schaeffer expression (Scheaffer, 1987):

$$\mu_{s,fr} = \frac{p_s \sin\Phi}{2\sqrt{I_{2D}}} \tag{15}$$

where p_s is the solids pressure, Φ is the angle of internal friction, I_{2D} and is the second invariant of the deviatoric stress tensor.

2.3.7 Limit packing fraction

The maximum value for the volume fraction of the granular phase is specified. For monodisperse spheres, the packing limit is approximately 0.63.

2.3.8 Elastic modulus

It is defined as:

$$G = \frac{\partial P_s}{\partial \alpha_s} \tag{16}$$

for $G \geq 0$.

2.3.9 Models for interactions between phases

2.3.9.1 Drag coefficient

The Gidaspow model is a combination of the Wen and Yu model (Wen & Yu, 1966) and the Ergun equation (Ergun, 1949). When $\alpha_l > 0.8$, the exchange coefficient between the solid and liquid phase, K_{ls}, is defined as follows:

$$K_{sl} = \frac{3}{4} C_D \frac{\alpha_s \alpha_l \rho_l |\overline{v}_s - \overline{v}_l|}{d_s} \alpha_l^{-2.65} \tag{17}$$

Here, the drag coefficient is given by:

$$C_D = \frac{24}{\alpha_l Re_s}\left[1 + 0.15\,(\alpha_l Re_s)^{0.687}\right] \tag{18}$$

2.3.9.2 Turbulent dispersion

For turbulent multiphase flows using the Eulerian model, the effects of turbulent dispersion forces, which explain the transfer of momentum between phases, can be taken into account. The turbulent dispersion force acts as turbulent diffusion in dispersed flows.

2.3.9.3 Simonin model

$$\overline{F}_{td,q} = -\overline{F}_{td,p} = C_{TD} K_{pq} \frac{D_{t,pq}}{\sigma_{pq}} \left(\frac{\nabla \alpha_p}{\alpha_p} - \frac{\nabla \alpha_q}{\alpha_q} \right) \tag{19}$$

Here, σ_{pq} is the default dispersion Prandtl number 0.75. K_{pq} is the interaction coefficient between the phases, $\nabla\alpha_p$ and $\nabla\alpha_q$ are the gradients of the volume fraction of the discrete phase and the continuous phase, respectively. C_{TD} is a constant equal to 1 by default.

3 Results and discussion

3.1 Volume fraction contours and fluidization regimes for particles of different diameters

Figure 4 shows the axial contours of the ilmenite volume fraction in a vertical plane that cuts through the middle of the mathematical domain, using different particle sizes. If 80 μm particles are used (Figure 4a), it can be observed that the granular phase is carried out of the system by the gas phase, both in the air reactor and the fuel reactor; in regions (1) and (2), it can be seen that the flow lines for the granular phase at the cyclone separator and fuel reactor outlets, respectively, show that the particles leave the system through the cyclone and fuel reactor outlets. Therefore, using this particle size for the given operating and boundary conditions is not feasible. In the case of particles with a diameter of 120 μm (Figure 4b), the volume fraction contour reveals an absence of the granular phase in the air reactor, as the granular phase is wholly carried away. However, in region (3)., the flow lines show that not all granular phase leaves the system through the air reactor outlet.

On the other hand, in the fuel reactor, the volume fraction contour shows a higher level of the granular phase, confirming that a large portion of the granular phase from the air reactor passed into the fuel reactor. At the same time, the flow lines in region (4) also show that most of the granular phase is not leaving the system through the air reactor. When using 150 μm particles (Figure 4c), the volume fraction contour shows a turbulent fluidization regime with pneumatic transport of particles throughout the air reactor. In contrast, a bubbling fluidization regime is observed in the fuel reactor and the pot-seal. In regions (5) and (6), the flow lines indicate that the gas carries the granular phase in the air reactor. Subsequently, in the cyclone, most of the particles fall into the fuel reactor, indicating that this particle size is suitable for the CLC system, as it allows particles to pass from

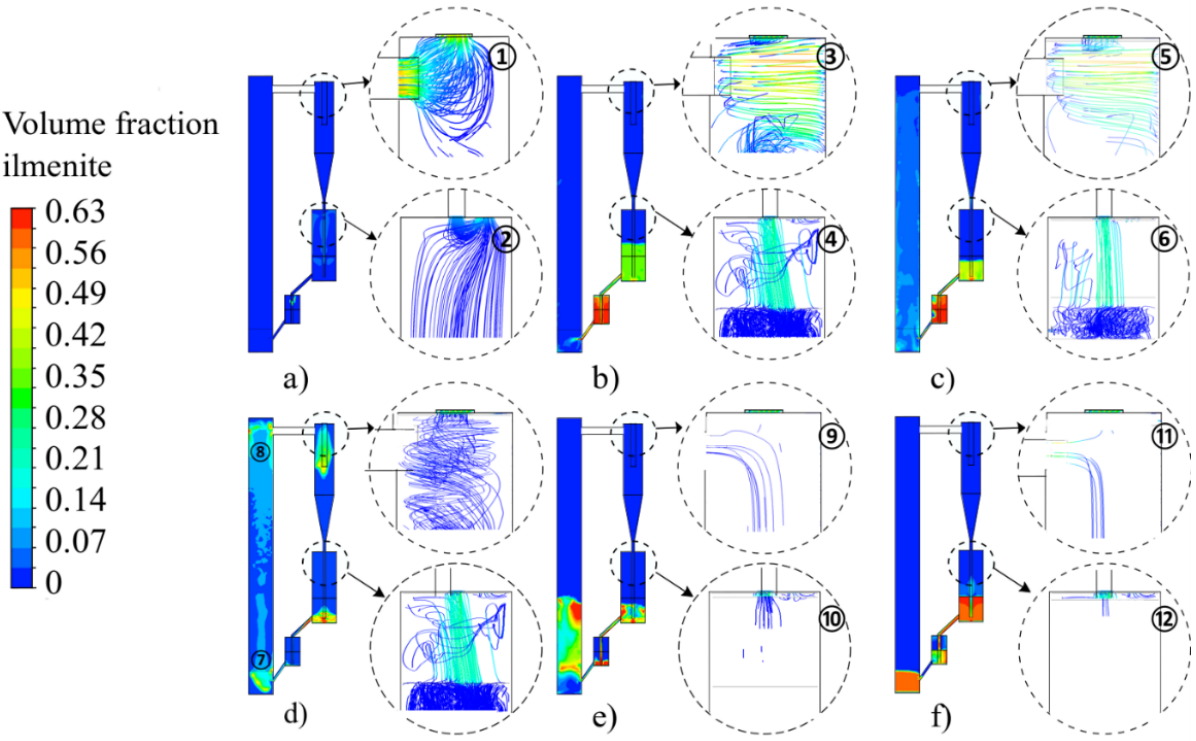

Figure 4. Axial volume fraction contours of ilmenite at 30 s after the start of the simulation and close-ups of particle path lines colored by velocity. a) 80 μm, b) 120 μm, c) 150 μm, d) 180 μm, e) 220 μm, f) 270 μm.

one reactor to another through pneumatic transport. On the other hand, in the fuel reactor, a bubbling fluidized bed regime is maintained, facilitating contact between the granular and gas phases. In the case of using 180 μm particles (Figure 4d), in regions (7) and (8), a behavior similar to the 'flat slugging' regime is observed, with particles forming agglomerations that hinder pneumatic transport.

Meanwhile, in the fuel reactor and the sealing bed, a low level of the granular phase is noted, as gravity causes the particles to move downward. The flow lines indicate behavior similar to that observed for 150 μm diameter particles. Finally, when using 220 μm particles (Figure 4e) or 270 μm (Figure 4f), it can be seen that the granular phase is in a minimum fluidization regime throughout the CLC system, which prevents the transport and exchange of particles between the air reactor and the fuel reactor. This can be confirmed by the volume fraction contour and the flow lines shown in regions (9), (10), (11), and (12), as a minimal granular phase is observed in the cyclone separator. Similarly, there is very little presence of granular phase entering the fuel reactor through the cyclone separator.

The fluidization regime that most favors the oxidation reactions of ilmenite in the air reactor is the turbulent fluidization regime with pneumatic drag, as it allows for better interaction between both phases. Meanwhile, the bubbling fluidization regime in the fuel reactor is the most suitable for reducing ilmenite particles. This regime allows for contact between the phases but prevents the drag of the granular phase. The behavior described above corresponds to particles with a diameter of 150 μm. In Figure 5, the cross-sectional volume fraction contours are analyzed. When using particles of 80 μm (Figure 5a) or 120 μm (Figure 5b), a low presence of the granular phase is observed, similar to what is seen in the axial contours (Figures 4a and 4b). When the particles in the system are 150 μm, a better distribution of particles is also noted, as seen in the axial contour profiles (Figure 4c). Suppose 180 μm particles are used (Figure 5d). In that case, a considerable presence of the granular phase is observed in the cross-section, and this concentration of particles corresponds to what is shown in the axial profiles (Figure 4d); however, this high concentration of the granular phase is not maintained throughout the air reactor, as can be seen in the axial contour of the vertical plane in Figure 4d, which shows regions with low particle concentration. When using 220 μm particles (Figure 5e), a central region is observed with no presence of the granular phase, and around it, a region with low particle concentration, clearly indicating no good fluidization regime. Finally, in Figure 5(f), it can be seen that the granular phase occupies the space shown in the contour of the plane

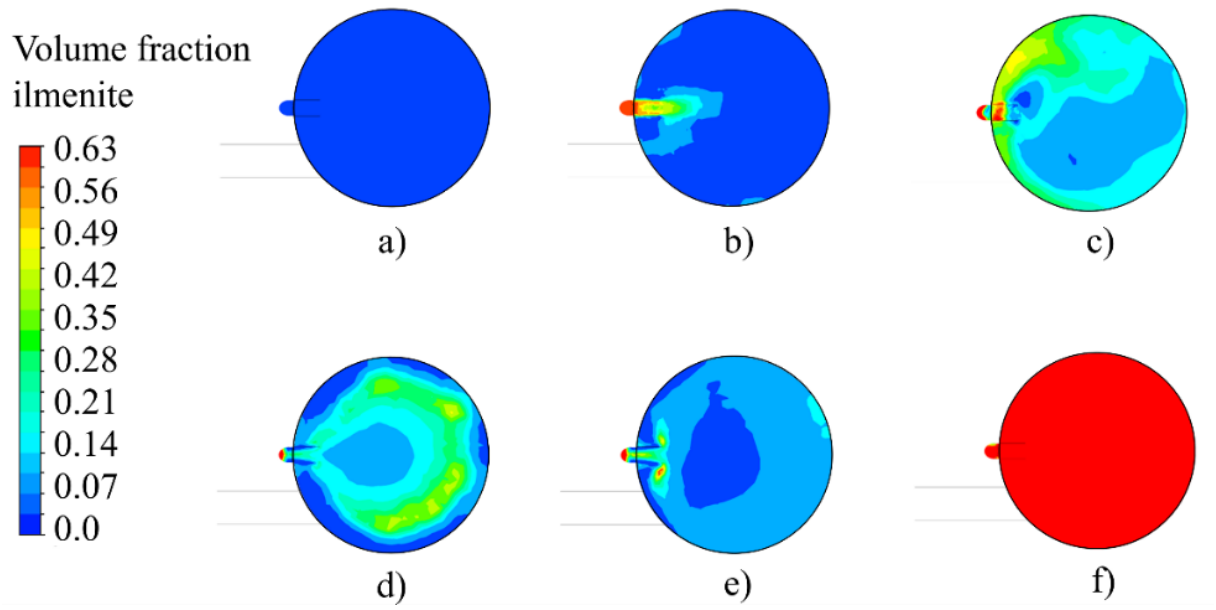

Figure 5. Cross-sectional volume fraction contours of ilmenite at 30 seconds after startup, in the cross-section at 0.1 m from the bottom of the air reactor a) 80 μm, b) 120 μm, c) 150 μm, d) 180 μm, e) 220 μm, f) 270 μm.

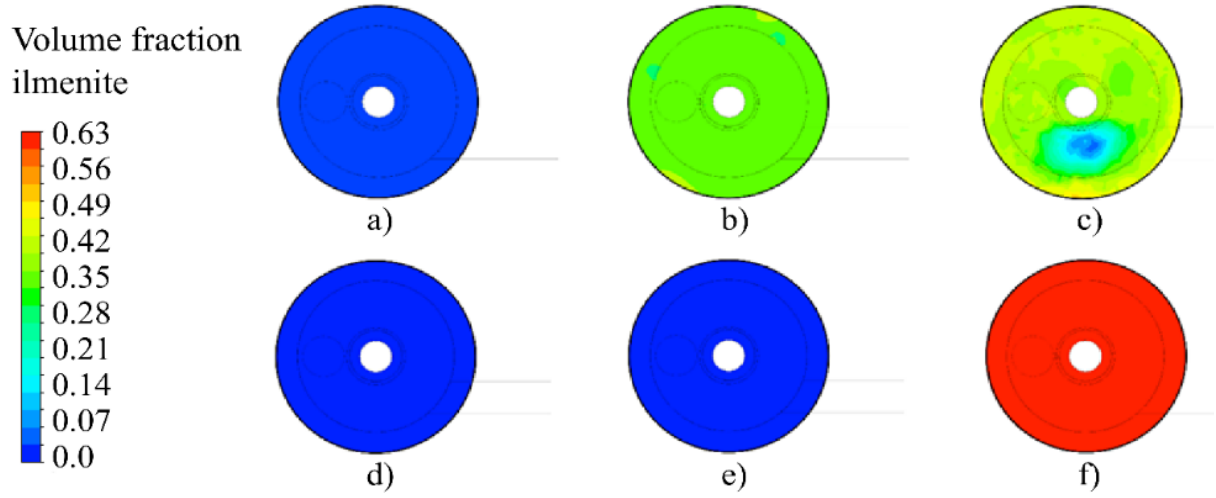

Figure 6. Volume fraction contours of ilmenite at 30 seconds, in cross-section at 0.1 m from the bottom of the fuel reactor. a) 80 μm, b) 120 μm, c) 150 μm, d) 180 μm, e) 220 μm, f) 270 μm.

due to gravitational forces exceeding drag forces, leaving the granular phase at the bottom of the air reactor.

The cross-sectional volume fraction contours of ilmenite in the fuel reactor show that when using 80 μm particles (Figure 6a), there is no concentration of the granular phase due to the strong drag caused by the gas phase. When using larger diameter particles, such as 120 μm (Figure 6b) or 150 μm (Figure 6c), the presence of the granular phase is observed, confirming that the fluidized bed regime is achieved. However, when attempting to use larger diameter particles, such as 180 μm (Figure 6d) or 220 μm (Figure 6e), there is no granular phase, as the particles have mainly moved toward the sealing bed. In the case of using 270 μm particles (Figure 6f), the behavior of the minimum fluidization regime is reaffirmed.

3.2 *Particle distribution and average axial velocity profile for particles of different diameters*

In Figure 7, the particle distribution profiles are analyzed at three different heights: 0.5 meters, 0.8 meters, and 1.5 meters. At 0.5 meters in height (Figure

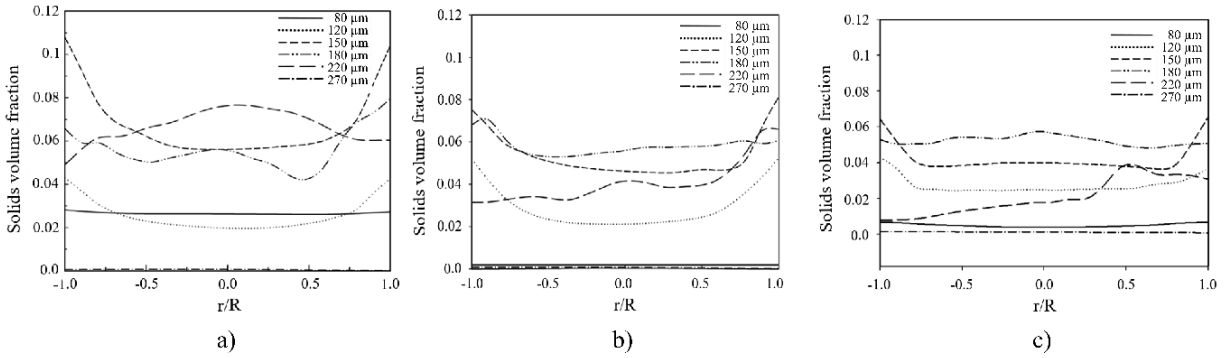

Figure 7. Particle distribution at different heights in the air reactor. a) 0.5 m, b) 0.8 m and c) 1.5 m.

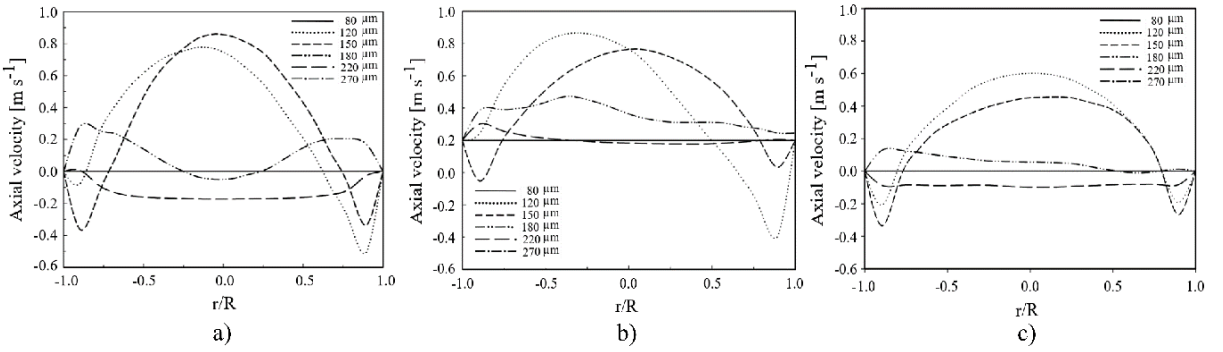

Figure 8. Velocity profiles at different heights in the air reactor. a) 0.5 m, b) 0.8 m and c) 1.5 m.

7a), the profile varies for each size. The curve for 80 μm particles is nearly horizontal with a low volume fraction. The distribution of 120 μm particles shows a volume fraction similar to that of 80 μm particles; however, the profile is not horizontal but concave, indicating a higher concentration of the granular phase near the walls. The 150 μm particles also exhibit a concave profile but with a greater concentration than the 120 μm particles. This particle distribution profile is similar to that obtained in previous studies for diameters of 150 μm (Guan, Chang, Zhang, Wang, & Sun, 2014; Shuai W. *et al*., 2011). The distribution observed for the 180 μm particles is similar to that of the 150 μm curve. In the 220 μm particle distribution curve, a slight increase in the concentration of the granular phase is observed in the central region of the air reactor; however, the profile is slightly convex. The volume fraction curve for 270 μm particles is zero, as the airflow does not carry these particles. At 0.8 meters height (Figure 7b), the particle distribution is similar to that observed in the graph at 0.5 meters (Figure 7a). The particles with diameters of 120 μm and 150 μm exhibit concave profiles, being more significant with a solid fraction of the 150 μm curve. At 1.5 meters height, the same trend is observed for the granular phase concentration profiles as those shown at 0.8 meters, as seen in Figure 7c; however, they differ in the concentration of the granular phase, as at 1.5 meters height, the volume fraction of solids decreases slightly.

On the other hand, Figure 8 shows the axial velocity profiles, which, at a height of 0.5 m (Figure 8a), exhibit convex curves for the 120 μm and 150 μm particles. These curves reveal an upward behavior in the central region of the air reactor, while negative velocities are observed near the walls, indicating a downward movement. These profiles correspond to those reported in the work of Guan *et al*. (Guan, Chang, Zhang, Wang, & Sun, 2014). The profiles for the other diameters are close to zero. The axial velocity profile at 0.8 m height (Figure 8b) is similar to that shown for 0.5 m height. It can be seen that, again, the curves for the 120 μm and 150 μm particles maintain a convex profile; however, a decrease in the maximum velocity achieved by the granular phase is observed. The axial velocity profiles at 1.5 m height (Figure 8c) remain unchanged from the previous heights; however, a decrease in the axial velocity of the particles is noticeable, and again, the profile shown by the 120 μm and 150 μm particles is similar to those reported in previous studies (Guan, Chang, Zhang, Wang, & Sun, 2014; Shuai W. *et al*., 2011). Such a profile can also be observed in the results presented by Lin et al. (2019), where negative velocities are shown near the walls, while the maximum velocity is observed in the central region, as demonstrated in this study for 150 and 120–micron particles.

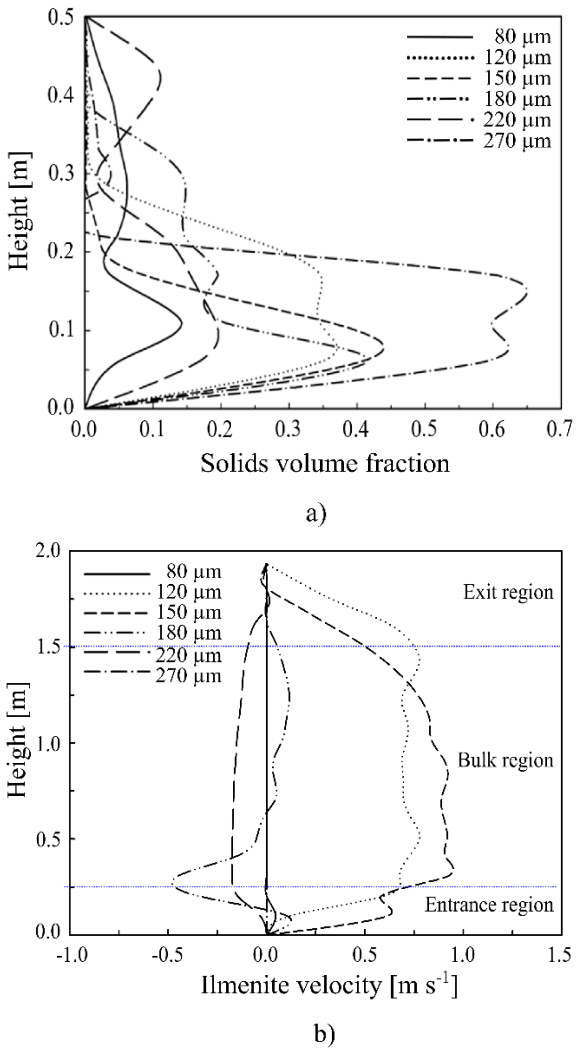

Figure 9. a) Particle distribution profiles in the fuel reactor, b) Velocity profiles of the granular phase throughout the air reactor.

These studies help validate the velocity profiles found in this numerical simulation.

In Figure 9a), the distribution of particles in the fuel reactor can be observed. The graph shows that, in general, for all particle diameters, the fluidized bed is located below 0.22 meters in height. However, there are apparent differences in the distribution of particles of different diameters. The 270 μm particles show a high concentration below 0.2 meters due to the fact that the airflow hardly fluidizes the bed. The 120 μm, 150 μm, and 180 μm particles show similar distributions below 0.2 meters, with maximum volume fractions of 0.44. This behavior is advantageous as it allows for a more significant volume fraction for the gas phase, leading to better conditions for the combustion reaction. However, having high volume fraction values in higher regions of the fuel reactor is undesirable, as this could cause particles to be dragged out of the system. In this regard, the 150 μm particles have the lowest volume fraction above 0.2 m in height. Regarding the 80 μm and 220 μm particles,

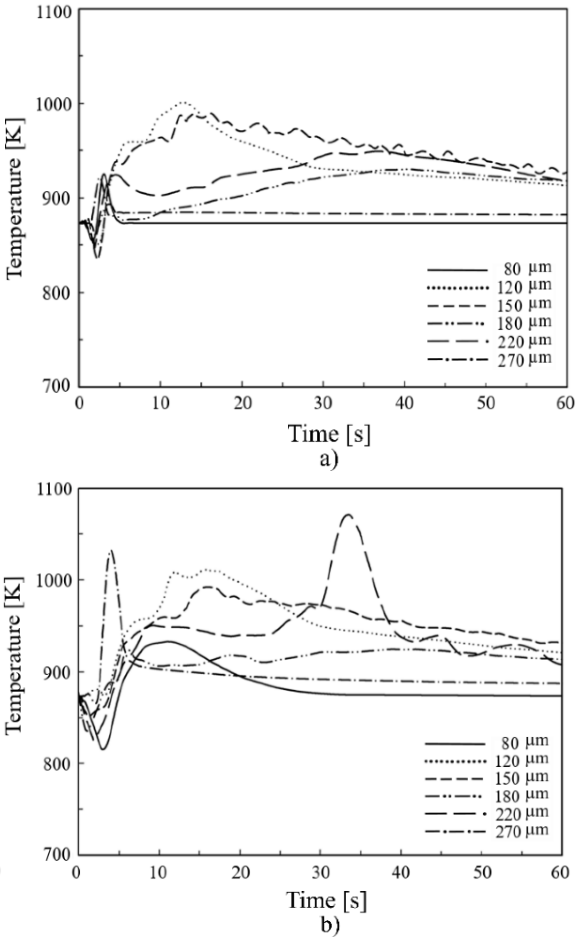

Figure 10. Temperature profiles. a) cyclone outlet, b) fuel reactor outlet.

a maximum volume fraction of 0.2 is observed, which is not ideal as it may affect the combustion reaction. The results in the fuel reactor shown by the profiles in Figure 9a) again indicate that the 150 μm diameter particles exhibit the most suitable behavior within the fuel reactor. This particle size aligns with what Sornumpol *et al.* reported (Sornumpol, Uraisakul, Kuchonthara, Chalermsinsuwan, & Piumsomboon, 2017), who concluded through an experimental design that the best particle size corresponds to 150 μm. On the other hand, the velocity profiles of the granular phase throughout the air reactor are shown in Figure 9b), where it is evident that the 120 μm and 150 μm particles are satisfactorily fluidized. These profiles are similar to those obtained in the work of Guan *et al.* (Guan, Chang, Zhang, Wang, & Sun, 2014). As in that study, the 120 μm and 150 μm profiles exhibit three regions: an inlet region, a bulk region, and an outlet region, as can be seen in Figure 9b).

3.3 Analysis of thermal results within the CLC system

Figures 10a) and 10b) show temperature profiles at the outlets of the cyclone separator and the fuel

reactor, respectively, for different particle diameters. In both figures, it can be observed that the system that best conserves heat corresponds to the 150 μm diameter particles. The cases that show the greatest cooling correspond to the 80 μm and 270 μm diameter particles. The 120 μm, 180 μm, and 220 μm particles show final temperatures that are very close to each other; however, all are below the final temperature of the 150 μm particle system. These temperature profiles suggest that the appropriate fluidization regimes for the granular phase, both in the air and fuel reactors, help reduce heat losses through the system outlets. In contrast, systems with poorer fluidization regimes exhibit temperature profiles with more significant cooling. Including chemical reactions in the system would affect these temperature profiles by introducing heat generation or absorption depending on the nature of the reactions. Exothermic reactions could generate higher temperatures in the fuel reactor, especially in systems with efficient fluidization. At the same time, endothermic reactions in the air reactor could lower the temperature, particularly in systems with poor fluidization, where heat transfer is less effective. Including these reactions would also affect heat distribution and the dynamics of the flows within the reactors, possibly altering the fluidization behavior and the temperature profiles observed in this simulation. Therefore, the role of chemical reactions could be significant in optimizing the thermal balance and improving the overall system efficiency. However, this work determined the analysis of particle sizes suitable for fluid dynamic phenomena within reactors; that is, to obtain a homogeneous dispersion of particle-gas flow. This study lays the foundation for future work involving chemical reactions since, being a surface phenomenon, the results obtained in this work determine the optimal gas-particle contact areas.

3.4 Modelling perspectives

As shown, momentum, mass, and energy balances are possible to solve using CFD software for different particle sizes and feedstocks. Nevertheless, the system's actual behavior could be better known because this model inferred the movement of the particles inside the reactor using supported correlations instead of experimental data. Due to their advantages in high mass and heat transfer rates and the vigorous mixing of solids that provokes good gas-solids contact, both reactors were considered solid-gas fluidized beds. However, any problem related to poor solid mixing, undesirable gas flow patterns, or physical operating problems will provoke a decrease in reactor performance (Shafiq, Azam, & Hussain, 2021). The hydrodynamic behavior of gas-solid fluidized beds varies with scale. When scaling up fluidized bed reactors, the behavior of large-scale fluidized beds usually differs significantly from the lab-scale behavior (Efhaima & Al-Dahhan, 2017) and, more severely, from the CSTR model (Levesnpiel, 1999). Therefore, it is essential to identify the experimental conditions that can provide similar and non-similar radial profiles of the gas holdup in the used beds to properly assess the new mechanistic scale-up of gas-solid fluidized beds (Efhaima & Al-Dahhan, 2021). In order to solve these uncertainties intrinsic to the scale-up procedure, Zaid and Al-Dahan (Zaid, Al-Rubaye, Aljuwaya, & Al-Dahhan, 2023) have recently proposed to group all the important parameters related to mechanical and thermal energy as well as to the geometry of particles and reactors into dimensionless numbers. This group completes the previous proposition of dimensionless groups (Glicksman, Hyre, & Woloshun, 1993). This approach seems very promising because mass and energy balances can be derived from the momentum balances, once the particle movement inside the reactor is known (Whitaker, 2009).

Conclusions

A 3D model of a combustion process in chemical cycles was developed using CFD, incorporating the kinetic theory of granular flow to study the effect of particle diameter on its behavior within the system. The results of this study showed the following:

1. Particle diameter significantly influences particle distribution in the fuel and air reactors, as different fluidization regimes develop depending on the particle diameter.

2. The distribution of particles and the velocity profile in the air reactor at different heights demonstrate that, according to previous reports, diameters of 120 μm and 150 μm achieve the most suitable profiles.

3. The velocity profiles throughout the air reactor are most suitable for the 120 μm and 150 μm particles. These profiles exhibit three defined regions: an inlet region, a bulk region, and an outlet region; this behavior has also been reported in previous studies.

4. In the fuel reactor, for the six different diameters, most of the particles are located below 0.2 m in height; however, the best distribution was obtained for the 120 μm, 150 μm, and 180 μm particles.

5. Regarding the temperature profiles, the results show less cooling in the combustion system in chemical cycles with 150 μm diameter particles.

Based on the evaluation of fluidization regimes, particle distribution, and thermal conservation, the use of 150 μm diameter particles in CLC systems is recommended, as they ensure a balance between pneumatic transport, phase contact, and thermal efficiency, improving the performance of the system in terms of conversion and operational stability. Generally, it can be concluded that, for the conditions of velocity, pressure, and temperature (shown in Table 3), particles with diameters of 150 μm exhibit better performance in particle distribution, velocity, and temperature profiles.

Acknowledgements

The authors thank the support of project 20.20-CIC-UMSNH, TecNM for the use of facilities, FAOV thanks for the CONACYT scholarship 956195, and CAHB, GJG, JARB, and RMY thank for the CONACYT-SNI scholarships. The authors would like to extend their thanks to Dr. Gildardo Solorio Díaz for his support in using ANSYS software.

Nomenclature

α_q	Volume fraction of phase q
ρ_q	Density of phase q, kg/m^3
$\vec{v}_q$	Velocity vector of phase q, m/s
m_{pq}	Mass transfer rate from phase p to phase q, kg/s
S_q	Mass source term, kg/s
P	Pressure shared between phases, Pa
τ_q	Stress tensor of phase q, Pa
μ_q	Stress tensor of phase q, Pa ·s
λ_q	Bulk viscosity of phase q. Pa·s
g	Gravitational acceleration, m/s^2
h_q	Specific enthalpy of phase q, J/kg
$\overline{q}$	Heat flux, W/m^2
G_k	Generation of turbulent kinetic energy, m^2/s^3
G_b	Generation of turbulent kinetic energy by buoyancy, m^2/s^3
e_{ss}	Coefficient of restitution in particle collisions
θ_s	Granular temperature of the solid phase, m^2/s^2
g_0	Radial distribution function
d_s	Particle diameter of the solid phase, m
$F_{td,q}$	Turbulent dispersion force for phase q, N
C_D	Drag coefficient
$\mathrm{Re_s}$	Reynolds number of the solid phase
σ_{pq}	Dispersion Prandtl number
C_{TD}	Turbulent dispersion constant
Φ	Angle of internal friction, degrees
I_{2D}	Second invariant of the deviatoric stress tensor
G	Elastic modulus of the granular material, Pa

References

Adanez , J., Abad, A., Garcia-Labiano, F., Gayan, P., & De Diego, L. (2012). Progress in chemical-looping combustion and reforming technologies. *Progress in energy and combustion science, 38*(2), 215-282. doi: https://doi.org/10.1016/j.pecs.2011.09.001

ANSYS. (2013). Ansys Fluent Theory Guide. *Theory Guide*. Retrieved from Retrieved from https://www.ansys.com

Archer, C., & Jacobson, M. (2005). *Journal of Geophysical Research: Atmospheres*, 110(D12). doi: https://doi.org/10.1029/2004JD005462

Deng, Z., Xiao, R., Jin, B., & Song, Q. (2009). Numerical simulation of chemical looping combustion process with $CaSO_4$ oxygen carrier. *International Journal of Greenhouse Gas Control, 3*(4), 368-375. doi: https://doi.org/10.1016/j.ijggc.2008.11.004

Deng, Z., Xiao, R., Jin, B., Song, Q., & Huang, H. (2008). Multiphase CFD modeling for a chemical looping combustion process (fuel reactor). *Chemical Engineering & Technology, 31*(12), 1754-1766. doi: https://doi.org/10.1002/ceat.200800341

Efhaima, A., & Al-Dahhan, M. (2017). Assessment of scale-up dimensionless groups methodology of gas-solid fluidized beds using advanced non-invasive measurement techniques (CT and RPT). *The Canadian Journal of Chemical Engineering, 95*(4), 656-669. doi: https://doi.org/10.1002/cjce.22745

Efhaima, A., & Al-Dahhan, M. (2021). Validation of the new mechanistic scale-up of gas-solid fluidized beds using advanced non-invasive measurement techniques. *The Canadian Journal of Chemical Engineering, 99*(9), 1984-2002. doi: https://doi.org/10.1002/cjce.23938

Ergun, S. (1949). Fluid Flow through Randomly Packed Columns and Fluidized Beds. *Industrial & Engineering Chemistry, 41*(6), 1179-1184. doi: https://doi.org/10.1021/ie50474a011

Gitay, H. (2002). Biodiversity IPCC Technical Paper. *Change Climate*.Glicksman, L., Hyre, M., & Woloshun, K. (1993). Simplified scaling relationships for fluidized beds. *Power*

Technology, 77, 177-199. doi: https://doi.org/10.1016/0032-5910(93)80055-F

Guan, Y., Chang, J., Zhang, K., Wang, B., & Sun, Q. (2014). Three dimensional CFD simulation of hydrodynamics in an interconnected fluidized bed for chemical looping combustion. *Powder technology 268*, 316-328. doi: https://doi.org/10.1016/j.powtec.2014.08.046

Höök, M., & Tang, X. (2013). Depletion of fossil fuels and anthropogenic climate change—A review. Energy policy. *Energy policy, 52*, 797-809. doi: https://doi.org/10.1016/j.enpol.2012.10.046

Jin, B., Xiao, R., Deng, Z., & Song, Q. (2009). Computational fluid dynamics modeling of chemical looping combustion process with calcium sulphate oxygen carrier. *International Journal of Chemical Reactor Engineering, 7*(1). doi: https://doi.org/10.2202/1542-6580.1786

Jung, J., & Gamwo, I. (2008). Multiphase CFD-based models for chemical looping combustion process: Fuel reactor modeling. *Powder Technology, 183*(3), 401-409. doi: https://doi.org/10.1016/j.powtec.2008.01.019

Kerr, H. (2005). Capture and separation technologies gaps and priority research needs. *Elsevier Ltd. Oxford, UK, 1*, 655-660.

Kruggel-Emden, H., Rickelt, S., Stepanek, F., & Munjiza, A. (2010). Development and testing of an interconnected multiphase CFD-model for chemical looping combustion. *Chemical engineering science, 65*(16), 4732-4745. doi: https://doi.org/10.1016/j.ces.2010.05.

Kumar, S., & Muhuri, P. (2019). A novel GDP prediction technique based on transfer learning using CO_2 emission dataset. *Applied Energy, 253*, 113476. doi: https://doi.org/10.1016/j.apenergy.2019.113476

Launder, B., & Spalding, D. (1983). The numerical computation of turbulent flows. *Numerical prediction of flow, heat transfer, turbulence and combustion*, 96-116. doi: https://doi.org/10.1016/B978-0-08-030937-8.50016-7

Levesnpiel, O. (1999). COMMENTARIES: Chemical Reaction Engineering. *Industrial and Engineering Chemistry Research, 38*, 4140-4143.

Lin, J., Luo, K., Sun, L., Wang, S., Hu, C., & Fan, J. (2019). Numerical investigation of nickel–copper oxygen carriers in chemical-looping combustion process with zero emission of CO and H_2. *Energy & Fuels*, *33*(11), 12096-12105.

Lun, C., Savage, S., Jeffrey , D., & Chepurniy, N. (1984). Kinetic theories for granular flow: inelastic particles in Couette flow and slightly inelastic particles in a general flowfield. *Journal of fluid mechanics, 140*, 223-256. doi: https://doi.org/10.1017/S0022112084000586

Mahalatkar, K., Kuhlman, J., Huckaby, E., & O'Brien, T. (2011). Computational fluid dynamic simulations of chemical looping fuel reactors utilizing gaseous fuels. *Chemical engineering science, 66*(3), 469-479. doi: https://doi.org/10.1016/j.ces.2010.11.003

Martínez-Prado, M. A. (2016). Estimación de las emisiones de gases de efecto invernadero para el estado de Durango, México. *Revista Mexicana de Ingeniería Química*, *15*(2), 575-601. https://rmiq.org/iqfvp/Pdfs/Vol.%2015,%20No.%202/IA3/RMIQTemplate.pdf

Masson-Delmotte, V., Zhai, P., Pörtner, H., Roberts, D., Skea, J., Shukla, P., . . . Pidcock, R. (2018). *Global Warming of 1.5 OC: An IPCC Special Report on the Impacts of Global Warming of 1.5° C Above Pre-industrial Levels and Related Global Greenhouse Gas Emission Pathways, in the Context of Strengthening the Global Response to the Threat of Climate Chang.* Geneva, Switzerland: World Meteorological Organization.

Nguyen, T., Seo, M., Lim, Y., Song, B., & Kim, S. (2012). CFD simulation with experiments in a dual circulating fluidized bed gasifier. *Computers & chemical engineering, 36*, 48-56. doi: https://doi.org/10.1016/j.compchemeng.2011.07.005

Pugazhendhi, A., Mathimani, T., Varjani, S., Rene, E., Kumar, G., Kim, S., & Yoon, J. (2019). Biobutanol as a promising liquid fuel for the future-recent updates and perspectives. *Fuel, 253*, 637-646. doi: https://doi.org/10.1016/j.fuel.2019.04.139

Scheaffer, D. (1987). Instability in the evolution equations describing incompressible granular flow. *Journal of differential equations, 66*(1), 19-50. doi: https://doi.org/10.1016/0022-0396(87)90038-6

Seo, M., Nguyen, T., Lim, Y., Kim, S., Park, S., Song, B., & Kim, Y. (2011). Solid circulation and loop-seal characteristics of a

dual circulating fluidized bed: experiments and CFD simulation. *Chemical engineering journal, 168*(2), 803-811. doi: https://doi.org/10.1016/j.cej.2011.01.041

Shafiq, H., Azam, S., & Hussain, A. (2021). Steam gasification of municipal solid waste for hydrogen production using Aspen Plus Simulation. *Discover Chemical Engineering, 1*(4), 1-16. doi: https://doi.org/10.1007/s43938-021-00004-9

Shuai, W., Guodong, L., Huilin, L., Juhui, C., Yurong, H., & Jiaxing, W. (2011). Fluid dynamic simulation in a chemical looping combustion with two interconnected fluidized beds. *Fuel Processing Technology, 92*(3), 385-393. doi: https://doi.org/10.1016/j.fuproc.2010.09.032

Shuai, W., Huilin, L., Feixiang, Z., & Guodong, L. (2014). CFD studies of dual circulating fluidized bed reactors for chemical looping combustion processes. *Chemical Engineering Journal, 236*, 121-130. doi: https://doi.org/10.1016/j.cej.2013.09.033

Shuai, W., Yunchao, Y., Huilin, L., Jiaxing, W., Pengfei, X., & Guodong, L. (2011). Hydrodynamic simulation of fuel-reactor in chemical looping combustion process. *Chemical Engineering Research and Design, 89*(9), 1501-1510. doi: https://doi.org/10.1016/j.cherd.2010.11.002

Sornumpol, R., Uraisakul, W., Kuchonthara, P., Chalermsinsuwan, B., & Piumsomboon, P. (2017). CFD simulation of fuel reactor in chemical looping combustion. *Energy Procedia, 138*, 979-984. doi: https://doi.org/10.1016/j.egypro.2017.10.096

Stocker, T., Qin, D., Plattner, G., Alexander, L., Allen, S., Bindoff, N., & Xie, S. (2013). Technical summary. In Climate change 2013: the physical science basis. Contribution of Working Group I to the Fifth Assessment Report of the Intergovernmental Panel on Climate Change. *Cambridge University Press*, 1535.

Syamlal, M., Rogers, W., & O'Brien, T. (1993). MFIX documentation theory guide. USA: USDOE Morgantown Energy Technology Center. doi: https://doi.org/10.2172/10145548

Wen, & Yu, C. (1966). Mechanics of fluidization., *62*, pp. p. 100-111.

Whitaker, S. (2009). Chemical Engineering Education: Making Connections at Interfaces. *Revista Mexicana de Ingeniería Química, 8*, 1-33. Retrieved from https://rmiq.org/iqfvp/Pdfs/Vol%208%20no%201/RMIQ_Vol_8_No_1_1.pdf

Zaid, F., Al-Rubaye, H., Aljuwaya, T., & Al-Dahhan, M. (2023). Assessment of the Dimensionless Groups-Based Scale-Up of Gas-Solid Fluidized Beds. *Processes, 11*(1). doi: https://doi.org/10.3390/pr11010168